This is the preprint of the following article:

Poberžnik, Matic, et al. "Surface phase diagrams of pristine and hydroxylated barium hexaferrite surfaces from first-principles atomistic thermodynamics." *Applied Surface Science* 637 (2023): 157890.

Which has been published in final form at:

Surface Phase Diagrams of Pristine and Hydroxylated Barium Hexaferrite Surfaces from First-Principles Atomistic Thermodynamics

Matic Poberžnik[a,*], Gabriela Herrero-Saboya[a], Darko Makovec[b], Darja Lisjak[b], Layla Martin-Samos[a]

[a] *CNR-IOM Democritos National Simulation Center, Istituto Officina dei Materiali, c/o SISSA, via Bonomea 265, IT-34136, Trieste, Italy*
[b] *Department for Materials Synthesis, Jožef Stefan Institute, Jamova 39, SI-1000, Ljubljana, Slovenia*

Abstract

Barium hexaferrite (BHF) is a ferrimagnet, whose hexagonal unit cell presents five iron crystallographic sites along the c-axis. At the nanoscale, BHF nanoparticles grow in the form of platelets, characterized by a low thickness along its principal magnetization axis (c-axis), displaying uniaxial magnetic anisotropy with the easy axis pointing perpendicular to the platelet. This unique property of BHF nanoplatelets has lead to a variety of novel applications, which often require surface functionalization. However, it has been observed that the nanoplatelets display two different surface morphologies depending on the stage/conditions of preparation. To ground these experimental observations, we employ the *ab initio* thermodynamics framework to perform a systematic investigation of the thermodynamic stability of BHF bulk terminations under a wide range of chemical conditions. We calculate the surface phase diagrams of pristine and hydroxylated bulk terminations along the c-axis. For pristine terminations, two different iron terminated surfaces are preferred: the barium containing 2b termination (Ba-rich conditions) and the $4f_2$ iron terminated surface (Ba-poor conditions). In the presence of water, the hydroxylated oxygen-terminated surfaces (12k-O) are identified as the most stable ones at Ba-poor conditions and low pH values, whereas the hydroxylated 2b surface is preferred at high pH and Ba-rich conditions.

Keywords: DFT, atomistic thermodynamics, barium hexaferrite, surface stability, hydroxylation

1. Introduction

Hexagonal ferrites or hexaferrites are hard ferrimagnets. They constitute the majority of magnetic materials produced and have a wide range of uses and applications [1]. Among these complex oxides, the M-type hexaferrites (where M = Sr, Ba or Pb) stand out for being stable compounds with a relatively high saturation magnetization at room temperature. They crystallize in a hexagonal unit cell with iron atoms occupying five characteristic crystallographic sites along the c-axis (Fig. 1a). According to their local symmetry (number and position of coordinating oxygens), they are classified as octahedral (2a, $4f_2$ and 12k sites), tetrahedral ($4f_1$ site), and trigonal bipyramidal (3b site).

At the nanoscale, barium hexaferrite (BHF) thin films have been deposited on sapphire [2, 3, 4] and employed as nanocomposites [5]. Moreover, BHF nanoparticles have been hydrothermally synthesized [6]. These nanoparticles display a platelet like morphology, with a low thickness along the crystal c-axis, and a much larger surface area along the *ab* plane, presenting a low thickness-to-area ratio. The BHF nanoplatelets exhibit a unique property; a uniaxial magnetic anisotropy with a magnetic easy axis perpendicularly aligned to the basal plane of the platelet [7]. Because of this feature, BHF nanoplatelet dispersions in liquid crystals have been used as the first ferromagnetic fluids [8]. Moreover, they have been used in a variety of different fields, ranging from engineering to medicine, *e.g.*, as spin-memory devices [9], contrast agents for bioimaging [10], etc. These versatile implementations however often require specific surface functionalisation [11, 12, 13].

In order to efficiently functionalize the nanoplatelets, an understanding of their surface morphology in different chemical environments is desired. To this end, their surface morphology was investigated with HAADF STEM imaging [7]. From these images, it was observed that the termination of the synthesized

---

platelets changes depending on the chemical environment. It was induced that depending on the solution conditions, entire atomic layers are washed/removed from the platelets, modifying the termination of the nanoparticles. Specifically, immediately after synthesis in basic and Ba excess conditions, the nanoplatelets were terminated with Ba containing basal planes. After washing away the excess Ba with dilute nitric acid, the 12k iron layer was discerned as the one closest to the surface of the nanoplatelet. Additionally, upon drying the washed nanoplatelets in vacuum and subsequently annealing them at 700 °C, the Ba containing basal plane was *recovered*.

Even if two surface terminations have been observed from HAADF STEM imaging, at least seven bulk terminations can *a priori* compete to be the most stable one (the five iron-terminated surfaces, plus two oygen terminated ones, see Fig.1). In this work, we construct an atomistic model for the BHF surfaces in order to elucidate the possibility of different chemical environments favoring specific surface morphologies of the platelets. In particular, we perform a systematic investigation of the relative stability of BHF surfaces within the well established *ab initio* thermodynamics framework [14].

After introducing the employed computational model of the BHF surfaces (Section 2), we estimate the relative stability of different bulk terminations by computing their surface free energies as a function of the oxygen and iron chemical potentials (Section 3). We then consider BHF surfaces in contact with an atmosphere of water and we evaluate how the surface stability is modified with the hydroxylation of the pristine terminations (Section 4). Finally, we employ the computational hydrogen electrode formalism [15], which allows us to determine the surface free energy as a function of the pH and the potential of the standard hydrogen electrode, U_{SHE}.

2. Computational model

All calculations were performed with the Quantum-ESPRESSO package for electronic structure calculations [16, 17]. We used the Perdew-Burke-Ernzerhof (PBE) exchange-correlation functional [18], employing a plane wave basis set with a kinetic energy cutoff of 50 Ry (500 Ry for the charge density cutoff) in combination with ultrasoft pseudopotentials [19, 20]. The Brillouin zone was integrated with a 4×4×1 Monkhorst-Pack grid [21]. Given that BHF bulk is
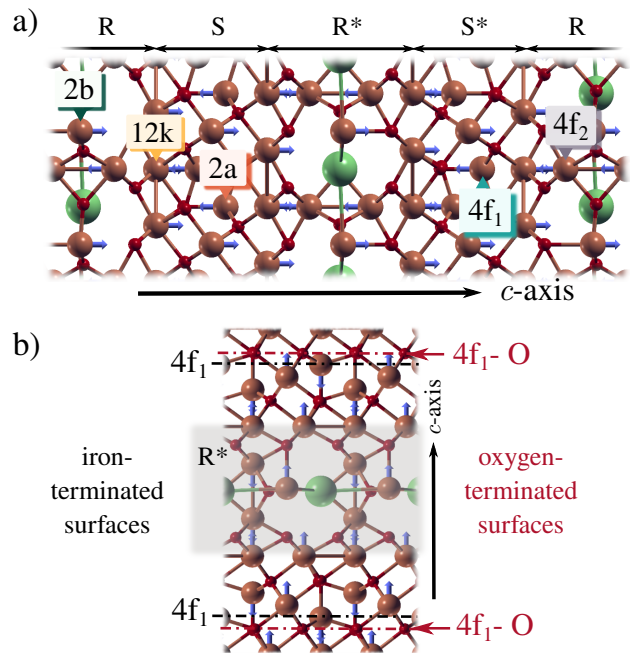

Figure 1: Model of the BHF surfaces. a) BHF bulk. The three chemical species are represented according to their atomic radii: barium is represented in green, iron in maroon and oxygen in red. The five crystallographic sites of the iron ions (2a, 2b, 12k, $4f_1$ and $4f_2$) are explicitly indicated, together with the characteristic R and S blocks. The blue arrows depict the majority *versus* minority spin contributions to the ferrimagnetic crystal. b) BHF bulk terminations. Two symmetric slabs with respect to the R* block are represented. In black, an iron-terminated slab, cut at the $4f_1$ crystallographic sites. In red, an oxygen-terminated surface, denoted as the $4f_1$-O termination.

ferrimagnetic, spin polarization is considered, and the starting magnetic moment (or majority *versus* minority spin contributions for each iron site) is set as predicted by Gorter [22] and represented in Fig. 1a. We account for the electronic localization in highly correlated materials by exploiting the DFT+U formalism [23]. In order to construct a parameter-free model, the on-site Coulomb repulsion or the U coefficient is estimated self-consistently, as indicated in [24]. For BHF bulk, an average U value of 4.3 eV is computed.

We calculate a total magnetization of 40 μ_{bohr} per unit cell, which is consistent with a contribution of 5 μ_{bohr} per iron ion and the spin distribution depicted in Fig. 1a. Note that a magnetic moment of 5 μ_{bohr} per iron ion is compatible with the maximal spin multiplicity of a Fe^{3+} cation. The computed magnetic moment is also in line with previous DFT+U calculations [25, 26, 27, 28, 29]. The BHF bulk unit cell is optimized by a volume cell minimization employing the DFT+U approach. The resulting lattice parameters, a = 6.00 Å and c =

23.52 Å, are in close agreement with experimental values [1]. Regarding its electronic structure, we obtain an electrical gap of 1.4 eV within the employed method, which is in line with experimental data [30].

Given the layered structure of BHF, it is safe to assume that the bulk terminations along the c-axis are the most representative and therefore they are the ones considered in this work. A BHF surface is approximated as a slab of the BHF unit cell subject to Periodic Boundary Conditions (PBC) for the basal directions and a vacuum layer of at least 15 Å along the main axis (or c-axis). The slab is cut from the crystal by two basal planes, imposing the same bulk termination for both surfaces. As represented in Fig. 1b, the slabs are symmetric with respect to an R block, presenting the same thickness above and below the referent core block. Two types of slabs are considered, depending whether the crystal is cut along planes containing iron atoms (iron-terminated surfaces) or along planes containing exclusively oxygen atoms (oxygen-terminated surfaces). The iron terminated surfaces are labelled according to the corresponding iron lattice sites (*e.g.* $4f_1$ in Fig. 1b), whereas the oxygen terminated ones take the name of the nearest iron layer (*e.g.* $4f_1$-O in Fig. 1b). In this work, we present a systematic investigation of all possible bulk terminations along the main axis, consisting on five iron-terminated slabs (the one with minimal width taken as the 2a termination) and two oxygen-terminated ones. Notice that because of the specific dimensions of the BHF nanoplatelets [7], our slab model for the BHF surfaces corresponds well to the observed thickness-to-area ratio of the particles. Border effects are therefore negligible and our results should align with experimental observations.

A 4×4×1 Monkhorst-Pack grid is employed for all considered slabs. The DFT+U method is exploited to evaluate the relative stability of the bulk terminations, and thus, we employ the U coefficient calculated for the BHF bulk ($U = 4.3$ eV). The dimensions of the unit cell are fixed according to the computed bulk lattice parameters. The starting magnetization of the slab is set according to the bulk spin distribution (Fig. 1a).

3. Relative stability of BHF bulk terminations

The most stable bulk termination is given by the lowest surface free energy, $\gamma(T, p, \mu_{Ba}, \mu_{Fe}, \mu_O)$, where T and p are the temperature and pressure of the environment and μ_{Ba}, μ_{Fe}, and μ_O are the chemical potentials of

barium, iron and oxygen atoms in the considered sample. Assuming a symmetric slab with two equivalent surfaces, the surface free energy can be written as,

$$\gamma(T, p, \mu_{Ba}, \mu_{Fe}, \mu_O) = \frac{1}{2A}[G_{slab}(T, p) - N_{Ba}\mu_{Ba}(T, p) - N_{Fe}\mu_{Fe}(T, p) - N_O\mu_O(T, p)], \quad (1)$$

where G_{slab} is the Gibbs free energy of the slab, N_{Ba}, N_{Fe}, and N_O are the number of barium, iron, and oxygen atoms in the considered slab, and μ_{Ba}, μ_{Fe}, and μ_O are the chemical potentials of the respective species, and A is the surface area. Given that the surfaces are in equilibrium with BHF bulk, the chemical potentials of the three constituents are related by the chemical potential of BHF bulk (μ_{BHF}),

$$\mu_{BHF} = \mu_{Ba} + 12\mu_{Fe} + 19\mu_O, \quad (2)$$

where the coefficients account for the stoichiometry of a bulk unit of BHF (BaFe$_{12}$O$_{19}$). Note that the temperature/pressure dependency of the chemical potentials is omitted in order to simplify the notation. The surface free energy can thus be written in terms of the chemical potentials of BHF bulk (μ_{BHF}), iron (μ_{Fe}), and oxygen (μ_O),

$$\gamma = \frac{1}{2A}\Big[G_{slab} - N_{BHF}\mu_{BHF}^{bulk} - (N_{Fe} - 12N_{BHF})\mu_{Fe} - (N_O - 19N_{BHF})\mu_O\Big], \quad (3)$$

where N_{BHF} is the number of bulk BHF units in the slab. Note that since $N_{BHF} = N_{Ba}$, the factors $(N_{Fe} - 12N_{BHF})$ and $(N_O - 19N_{BHF})$ account for the nonstoichiometry of the generated slab. This excess or deficit of iron or oxygen with respect to BHF bulk can result in the formation of *competing* compounds, i.e., oxides, molecular oxygen, and bulk metals. The chemical potentials of iron, oxygen and barium are therefore constrained to values where bulk BHF is the most stable specie. In the case of oxygen, the absolute upper limit for its chemical potential is set to that of molecular oxygen at atmospheric conditions,

$$\mu_O \leq \frac{1}{2}\mu_{O_2}^{gas}, \quad (4)$$

where $\mu_{O_2}^{gas}$ is the chemical potential of molecular oxygen at standard temperature-pressure conditions. In the case of the chemical potentials of barium and iron, the upper limit is set by their values in the bulk,

$$\mu_{Fe} \leq \mu_{Fe}^{bulk}, \quad \mu_{Ba} \leq \mu_{Ba}^{bulk}, \quad (5)$$

where μ^{bulk} stands for the Gibbs free energy per unit of bulk formula (for details see Section S1.1 in the Supplementary Material).

Moreover, when in contact with oxygen atmosphere, the two metals can also form oxides, such as BaO, Fe_2O_3 and Fe_3O_4. The chemical potentials are consequently further constrained,

$$
\begin{aligned}
\mu_{\text{Ba}} + \mu_{\text{O}} &\leq \mu_{\text{BaO}}^{\text{bulk}}, \\
2\mu_{\text{Fe}} + 3\mu_{\text{O}} &\leq \mu_{\text{Fe}_2\text{O}_3}^{\text{bulk}}, \\
3\mu_{\text{Fe}} + 4\mu_{\text{O}} &\leq \mu_{\text{Fe}_3\text{O}_4}^{\text{bulk}},
\end{aligned}
\tag{6}
$$

where μ^{bulk} stands for the Gibbs free energy per bulk unit of the respective oxide.

The boundary conditions defined in Eqs. 4,5 and 6 can also be rewritten uniquely in terms of μ_{BHF}, μ_{Fe}, and μ_{O}. Moreover, in order to ease the interpretation of the surface stability domains, we introduce the *deviations of chemical potentials*, defined as,

$$
\begin{aligned}
\Delta\mu_{\text{O}} &= \mu_{\text{O}} - \frac{1}{2}\mu_{\text{O}_2}^{\text{gas}}, \\
\Delta\mu_{\text{Fe}} &= \mu_{\text{Fe}} - \mu_{\text{Fe}}^{\text{bulk}}, \\
\Delta\mu_{\text{Ba}} &= \mu_{\text{Ba}} - \mu_{\text{Ba}}^{\text{bulk}}.
\end{aligned}
\tag{7}
$$

With these new definitions, $\Delta\mu_{\text{Fe}} \rightarrow 0$ and $\Delta\mu_{\text{O}} \rightarrow 0$ represent the upper limits of iron and oxygen rich conditions. The $\Delta\mu_i$ potentials are related by the Gibbs free energy of formation,

$$
\begin{aligned}
\Delta g_f(\text{BHF}) &= \mu_{\text{BHF}}^{\text{bulk}} - \mu_{\text{Ba}}^{\text{bulk}} - 12\mu_{\text{Fe}}^{\text{bulk}} - \frac{19}{2}\mu_{\text{O}_2}^{\text{gas}} \\
&= \Delta\mu_{\text{Ba}} + 12\Delta\mu_{\text{Fe}} + 19\Delta\mu_{\text{O}}.
\end{aligned}
\tag{8}
$$

The set of boundary conditions in Eqs. 4 and 5 read now,

$$
\begin{aligned}
\Delta\mu_{\text{O}} &\leq 0, \\
\Delta\mu_{\text{Fe}} &\leq 0, \\
12\Delta\mu_{\text{Fe}} + 19\Delta\mu_{\text{O}} &\geq \Delta g_f(\text{BHF}),
\end{aligned}
\tag{9}
$$

whereas the boundary conditions in Eq. 6 can be rewritten as,

$$
\begin{aligned}
12\Delta\mu_{\text{Fe}} + 18\Delta\mu_{\text{O}} &\geq \Delta g_f(\text{BHF}) - \Delta g_f(\text{BaO}), \\
2\Delta\mu_{\text{Fe}} + 3\Delta\mu_{\text{O}} &\leq \Delta g_f(\text{Fe}_2\text{O}_3), \\
3\Delta\mu_{\text{Fe}} + 4\Delta\mu_{\text{O}} &\leq \Delta g_f(\text{Fe}_3\text{O}_4),
\end{aligned}
\tag{10}
$$

where free energies of formation $\Delta g_f(\text{BaO})$, $\Delta g_f(\text{Fe}_2\text{O}_3)$ and $\Delta g_f(\text{Fe}_3\text{O}_4)$ have equivalent expressions as the one for BHF (Eq. 8). Their calculated

and experimental values are summarized in Table S2 in the Supplementary Material. The surface free energy is also expressed in terms of the deviations of chemical potentials,

$$
\begin{aligned}
\gamma = \frac{1}{2A} \big[\Phi_i &+ (N_{\text{Fe}} - 12N_{\text{BHF}})\Delta\mu_{\text{Fe}} \\
&+ (N_{\text{O}} - 19N_{\text{BHF}})\Delta\mu_{\text{O}}\big],
\end{aligned}
\tag{11}
$$

where,

$$
\begin{aligned}
\Phi_i = G_{\text{slab}} &- N_{\text{BHF}}\mu_{\text{BHF}}^{\text{bulk}} + (N_{\text{Fe}} - 12N_{\text{BHF}})\mu_{\text{Fe}}^{\text{bulk}} \\
&+ (N_{\text{O}} - 19N_{\text{BHF}})\frac{1}{2}\mu_{\text{O}_2}^{\text{gas}}.
\end{aligned}
\tag{12}
$$

The surface free energy in Eq. 11 is therefore written as a function of two variables, $\Delta\mu_{\text{Fe}}$ and $\Delta\mu_{\text{O}}$. The Φ_i function (Eq. 12) and the boundary conditions in Eq. 9 do however depend on the Gibbs free energy of the slab and a set of chemical potentials for bulk and gas species. In the case of periodic systems (*i.e.* the slab and the bulk materials), we estimate the free energies by DFT total energies per slab or unit cell respectively. By employing this approximation the pressure/volume and entropic contributions to the Gibbs free energy are neglected. The chemical potential for molecular oxygen at standard temperature-pressure conditions ($T_0 = 298$ K and $p_0 = 1$ atm) is approximated as the DFT total energy for an isolated oxygen molecule plus the thermal contributions to energy and entropy, which are computed as detailed in Section S1.2 and in the Supplementary Material. Moreover, assuming molecular oxygen behaves as an ideal gas, the pressure dependence of μ_{O} can be easily established as,

$$
\Delta\mu_{\text{O}} = kT\ln\frac{p}{p_0}.
\tag{13}
$$

From Eqs. 11 and 12, we calculate the surface free energy as a function of the deviation of the two chemical potentials, $\Delta\mu_{\text{O}}$ and $\Delta\mu_{\text{Fe}}$, for each of the considered bulk terminations. In Fig. 2, we show the most stable surface termination (the one with the lowest surface free energy) for each point in the $\Delta\mu_{\text{O}}$-$\Delta\mu_{\text{Fe}}$ plane. In the considered range of chemical potentials, two stability domains are found, corresponding to the bulk terminations 2b (shaded green) and 4f$_2$ (coloured grey). Note that bulk BHF is only stable within the limits of formation of the competing oxides (see Eq. 6). In Fig. 2, this stability region is shown in darker colors limited by black dotted lines, which correspond to the conditions where the competing oxides (BaO, Fe_3O_4, and Fe_2O_3) form. Notice that even within this narrow region where BHF is stable, there is a competition
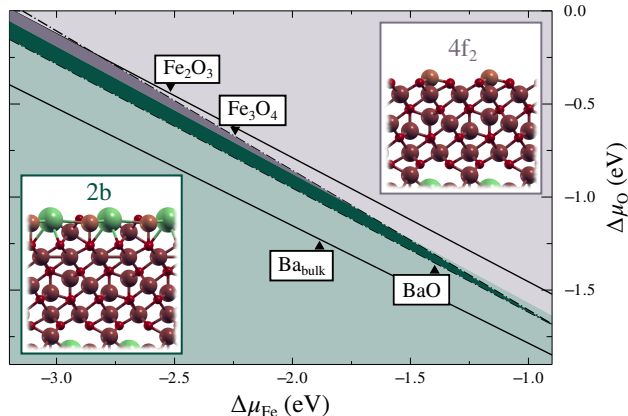
4

Figure 2: The most stable bulk termination for a given combination of the $\Delta\mu_{Fe}$ and $\Delta\mu_O$ potentials. The grey shaded region corresponds to the $4f_2$ termination, whereas the green coloured region represents the 2b termination. Black lines represent boundary conditions for the two chemical potentials above (below) which different species start to form, namely, bulk barium (Ba_{bulk}), barium oxide (BaO), magnetite (Fe_3O_4) and hematite (Fe_2O_3). Notice BHF is only stable in the region limited by dashed lines (or within the darker colored area). Side-views of the most stable terminations, 2b and $4f_2$ are also shown.

between the two surfaces.

As shown in Fig. 2, the $4f_2$ surface termination is the most stable slab for high values of both oxygen and iron chemical potentials, corresponding to oxygen/iron rich conditions. The 2b surface termination is found to be the most stable one for low values of both chemical potentials, corresponding to oxygen/iron poor conditions. Note that because the barium chemical potential is uniquely determined by the iron and oxygen potentials (Eq. 2), the decrease of μ_{Fe} and μ_O increases μ_{Ba} (Ba rich conditions), and conversely, the increase of μ_{Fe} and μ_O lowers μ_{Ba} (Ba poor conditions). We can thus summarize that the barium terminated 2b surface is preferred under Ba rich conditions, whereas the $4f_2$ surface is the preferred termination under Ba poor conditions.

This variation of surface stability with the presence of barium has been observed in the characterization of BHF nanoplatelts [7]. Indeed, different surface morphologies were identified from HAADF STEM imaging depending on the excess of barium in the solution. Right after the synthesis of the platelets, in Ba-rich conditions, an atomic surface layer containing Ba atoms was observed: the 2b termination. After washing away the excess of Ba with dilute nitric acid, the images show the nanoplatelets systematically terminate with an S-block or the 12-k termination. As stated by the authors [7], the 12k-O termination could also be compatible with the surface of the platelets, since the presence of oxygen in the 12-k layer could not be completely ruled out.

These observations might seem to partially contradict our prediction of the two most stable surfaces (Fig. 2). Our results correspond well with HAADF STEM images at Ba-rich conditions, whereas at Ba-poor conditions, we predict a different termination. Notice, however, that our computational framework does not take into account the presence of other species, such as water, which is almost unavoidable in a realistic experimental setup. Indeed, it has been shown that hydroxylation can alter the relative stability of the pristine terminations. To provide a quantitative comparison of the relative stability of pristine terminations for the BHF surfaces, we explicitly show the surface energies for all considered slabs as a function of the oxygen chemical potential (Fig. 3).

The values of the iron chemical potential are constrained to the formation of the oxides (or the boundary conditions in Eqs. 10). In the case of BaO, the chemical potential of iron is fixed to $\Delta\mu_{Fe} = \frac{1}{12}(\Delta g_f(BHF) - \Delta g_f(BaO) - 18\Delta\mu_O)$. In the case of the iron oxides, the iron chemical potential is constrained to the lowest value of either, $\Delta\mu_{Fe} = \frac{1}{2}(\Delta g_f(Fe_2O_3) - 3\Delta\mu_O)$, or, $\Delta\mu_{Fe} = \frac{1}{3}(\Delta g_f(Fe_2O_3) - 4\Delta\mu_O)$. Notice that these expressions correspond to dashed lines in Fig. 2. Throughout this article, these stability limits are referred to as stability or formation lines of the oxides. From the diagrams represented in Fig. 3, one can observe that the difference between the lowest surface free energies and the other terminations considered can become relatively small. For example, the surface free energy of the 12k-O termination is close to the most stable ones at oxygen rich conditions. Similarly, at low values of the oxygen chemical potential, the surface free energies of the 2a an 12k terminations approach the ones of the most stable 2b and $4f_2$ surfaces. In the following section, we therefore consider how the possibility of water dissociation and the corresponding different degrees of hydroxylation affect the relative stability of BHF bulk terminations.

4. The effect of hydroxylation

We now consider the set of BHF surfaces in contact with an atmosphere containing water. Water molecules can then be exchanged between the environment and the
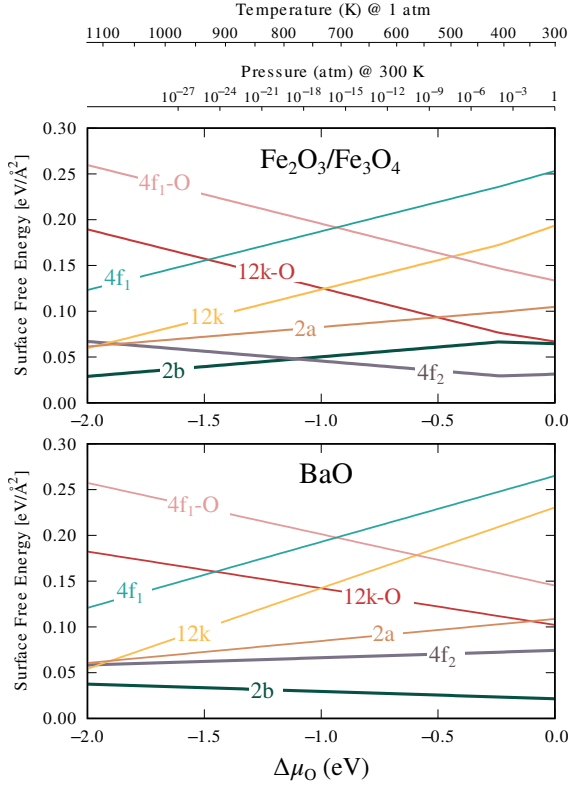
Figure 3: Surface free energies of the BHF slabs as a function of the oxygen chemical potential. In the upper panel, the iron chemical potential is fixed by the formation of iron oxides Fe_2O_3 and Fe_3O_4. In the lower panel, the surface free energies are constrained by the formation of BaO. Note that the values of the iron chemical potentials in these plots correspond to the stability limits represented by black lines in Fig. 2. For illustrative purposes, $\Delta\mu_O$ was also recast into a temperature scale at $p = 1$ atm and pressure scale at $T = 300$ K, using the ideal gas approximation.

surfaces, passivating the *pristine* bulk terminations. *A priori*, one can consider two modes of adsorption: the non-dissociative (plain) adsorption of a water molecule or the dissociative adsorption of a water molecule, where either hydrogen and/or a hydroxyl group are bonded to the surface after dissociation. We focus on the hydroxylation of the pristine BHF surfaces by considering the dissociative adsorption mode of water molecules on the particular termination. The nature of the chemical reaction (number of dissociated water molecules, products of the reaction, etc.) is therefore governed by the exposed *surface atoms* to which either the hydrogen atom or the hydroxyl group can bond. In the case of oxygen-terminated surfaces (*e.g.* the 12k-O termination), the water molecule dissociates with one hydrogen atom bonding to a surface oxygen atom (in order to create a surface hrydroxyl group), whereas the rest of the

water molecule is assumed to be released in the form of H_2 and O_2 into the environment,

$$H_2O + O* \rightarrow HO* + \frac{1}{2}H_2 + \frac{1}{2}O_2, \qquad (14)$$
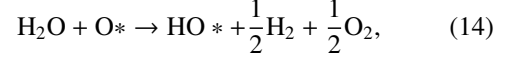
where $O*$ represents a surface oxygen atom at crystal site $*$ and $HO*$ is the resulting hydroxyl group at the same surface site. Alternatively, in the case of iron-terminated surfaces (*e.g.* the 2a termination), the water molecule can dissociate by forming a hydroxyl group bonded to a surface iron, where the remaining hydrogen leaves the system in the form of H_2, described by,

$$H_2O + * \rightarrow HO* + \frac{1}{2}H_2, \qquad (15)$$
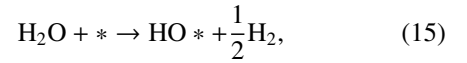
where $*$ represents an iron site and $HO*$ is the OH group bonded to that specific iron. Additionally, we consider a third scenario in which both iron and oxygen surface atoms are exposed to the environment. This is the case of the most stable clean surfaces, 2b and $4f_2$. As represented in Fig. 2, the 2b bulk termination exposes all three elements to the environment, whereas the $4f_2$ iron-terminated surface is characterised by an *uncovered* sub-layer of oxygen atoms. On these surfaces, water can dissociate by forming two surface hydroxyl groups, where hydrogen bonds to a surface oxygen and the hydroxyl group bonds to the surface iron,

$$H_2O + * + O* \rightarrow HO* + HO*. \qquad (16)$$
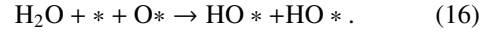
In this chemical reaction, $*$ denotes two different crystal sites, corresponding to the reactive iron and oxygen atoms. Notice that Eqs. 14, 15 and 16 represent the interaction between a BHF slab and one single water molecule. However, depending on the specific termination (number and nature of available sites), multiple water molecules can dissociate on the surface, representing different degrees of hydroxylation. Moreover, in order to ensure equivalent surfaces at both sides of the slab, we hydroxylate both surfaces symmetrically. With this approach we also avoid the spurious dipole that develops in the z direction of the periodic slab with nonequivalent surfaces.

In the following, we focus on the effect of hydroxylation on a subset of BHF slabs, according to their relative surface free energies with respect to the most stable slabs. In particular, the 12k, the $4f_1$ and the $4f_1$-O terminations will not be considered (see Fig. 3). Moreover, we consider the 12k-O slab at different degrees of hydroxylation; the adsorption of 1 to 4 H atoms per unit cell was considered since four

surface oxygen atoms are exposed in the unit cell. Regarding the iron-terminated surfaces, we include the 2a termination and the adsorption of one and two hydroxide groups per surface. Finally, we hydroxylate the 2b and $4f_2$ terminations, attaching one H atom and one OH group per surface.

Once the set of hydroxylated surfaces is built from Eqs. 14, 15 and 16, one needs to understand how the presence of water (and hydrogen) alters the surface free energies of the BHF bulk terminations. We therefore generalize expression 1 to include the dissociation of water molecules in the surfaces,

$$\gamma = \gamma_{\text{clean}} + \Delta\gamma_{\text{hyd}} \tag{17}$$

Where $\Delta\gamma_{\text{hyd}}$ represents the *gain* of hydroxylating a clean surface with $N_{\text{H}_2\text{O}}$ water molecules. For each of the chemical reactions 14, 15 and 16, one therefore needs to write $\Delta\gamma_{\text{hyd}}$ according to the dissociated water molecules. In the simplest case, the hydroxilation of iron-terminated surfaces or the 2a termination (equation 15), we define,

$$\Delta\gamma_{\text{hyd}} = \frac{1}{2A}\left[G_{\text{slab}}^{*\text{OH}} + N_{\text{H}_2\text{O}}\mu_{\text{H}} - G_{\text{slab}}^{\text{clean}} - N_{\text{H}_2\text{O}}\mu_{\text{H}_2\text{O}}\right], \tag{18}$$

where $G_{\text{slab}}^{*\text{OH}}$ is the Gibbs free energy of the hydroxylated slab, $G_{\text{slab}}^{\text{clean}}$ is the free energy of the corresponding clean slab, and $\mu_{\text{H}_2\text{O}}$ and μ_{H} are the chemical potentials of water and hydrogen respectively. Since we assume that both hydrogen and oxygen are in equilibrium with water, their chemical potentials are related as follows,

$$\mu_{\text{H}_2\text{O}} = 2\mu_{\text{H}} + \mu_{\text{O}}. \tag{19}$$

The gain in surface free energy due to hydroxylation of an iron-terminated surface can thus be expressed in terms of the oxygen and water chemical potentials,

$$\Delta\gamma_{\text{hyd}} = \frac{1}{2A}\left[G_{\text{slab}}^{*\text{OH}} - G_{\text{slab}}^{\text{clean}} - \frac{N_{\text{H}_2\text{O}}}{2}(\mu_{\text{H}_2\text{O}} + \mu_{\text{O}})\right]. \tag{20}$$

Equivalently, $\Delta\gamma_{\text{hyd}}$ for the hydroxylation of an oxygen-terminated surface, *e.g.*, the 12k-O termination, can be expressed as,

$$\Delta\gamma_{\text{hyd}} = \frac{1}{2A}\left[G_{\text{slab}}^{*\text{OH}} - G_{\text{slab}}^{\text{clean}} - \frac{N_{\text{H}_2\text{O}}}{2}(\mu_{\text{H}_2\text{O}} - \mu_{\text{O}})\right]. \tag{21}$$

Finally, in the case of having both oxygen and iron atoms exposed to the aqueous environment (he 2b and the $4f_2$ terminations), the gain in surface free energy is,

$$\Delta\gamma_{\text{hyd}} = \frac{1}{2A}\left[G_{\text{slab}}^{*\text{OH}} - G_{\text{slab}}^{\text{clean}} - N_{\text{H}_2\text{O}}\mu_{\text{H}_2\text{O}}\right]. \tag{22}$$

Once the expressions for $\Delta\gamma_{\text{hyd}}$ are induced for each of the Eqs. 14, 15 and 16, we are in the position of evaluating the surface stability domains for the new set of slabs. Notice that γ is now a function of the iron, oxygen and water chemical potentials. For simplicity, we drop the dependency on the iron chemical potential, taking μ_{Fe} as a function of μ_{O} along the formation of barium and iron oxides (dashed lines in Fig. 2). Moreover, we introduce the deviation of the chemical potential of water, analogous to the one for oxygen (Eq. 7),

$$\Delta\mu_{\text{H}_2\text{O}} = \mu_{\text{H}_2\text{O}} - \mu_{\text{H}_2\text{O}}^{\text{gas}}, \tag{23}$$

where $\mu_{\text{H}_2\text{O}}^{\text{gas}}$ is the chemical potential of water at standard temperature-pressure conditions. It is approximated as the DFT total energy of an isolated water molecule, corrected for the translational, rotational, and vibrational contributions to the thermal energy and entropy at $T = 298$ K and $p = 1$ atm, within the ideal gas and rigid rotor approximations (for details see Section S1.2 in the Supplementary Material). The surface free energy is hence written as a function of the *deviation* of two chemical potentials, $\Delta\mu_{\text{O}}$ and $\Delta\mu_{\text{H}_2\text{O}}$, whose upper limits are fixed by the formation of molecular oxygen and water in the gas-phase at standard conditions.

In Fig. 4, we show the surface with the lowest γ for each point in the $\Delta\mu_{\text{O}}$-$\Delta\mu_{\text{H}_2\text{O}}$ plane. Notice that besides the hydroxylated surfaces, the clean terminations discussed in Section 3 are also included. Along the BaO formation line, we distinguish three preferred surfaces, corresponding to the clean 2b termination, the hydroxylated 2b termination (OH+H@2b), and the fully hydroxylated 12k-O termination (with four hydrogen atoms per surface unit cell, labeled as 4H@12k-O in Fig. 4). As induced from Fig. 4, the stability regions in the $\Delta\mu_{\text{O}}$-$\Delta\mu_{\text{H}_2\text{O}}$ plane can be assigned to the oxygen rich *versus* oxygen poor conditions. The lack of oxygen in the system favors the presence of hydrogen, allowing the hydroxylation of the 12k-O surface. Additionally, the hydroxylated surfaces (OH+H@2b and 4H@12k-O are found to be more stable than the clean 2b surface at water rich conditions, whereas the clean surface is preferred in water poor conditions. Notice that the availability of hydrogen in the system (or μ_{H}) is not explicitly depicted in the $\Delta\mu_{\text{O}}$-$\Delta\mu_{\text{H}_2\text{O}}$ plane, but it can be induced from Eq. 19.

On the other hand, along the stability line corresponding to the formation of both iron oxides Fe_2O_3
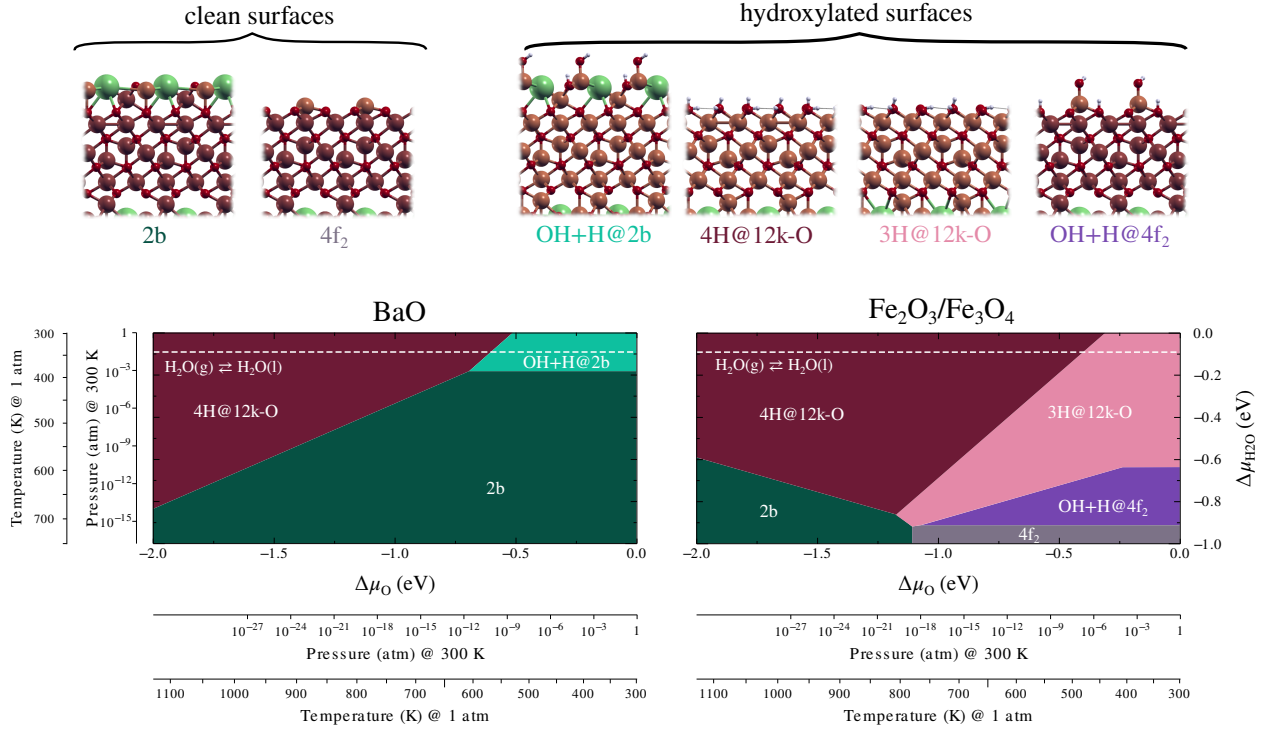
Figure 4: Stability domains of the clean and hydroxilated BHF surfaces. Colored regions in the lower panels represent terminations with the lowest surface free energy within a specific domain in the $\Delta\mu_O - \Delta\mu_{H_2O}$ plane. On the left panel, the 2b and the fully hydroxylated 12k-O terminations as the most stable surfaces in the $\Delta\mu_O - \Delta\mu_{H_2O}$ plane along the stability line corresponding to the formation of BaO. On the right panel, the clean 2b and the $4f_2$ terminations, together with the hydroxilated 4H@12k-O, 3H@12k-O and OH+H@4f_2 terminations as the most stable surfaces along the formation of the iron oxides. On the upper panel, side-views of the relevant surfaces within the considered ranges of the chemical potentials $\Delta\mu_O$ and $\Delta\mu_{H_2O}$. The white dashed lines indicate the value of $\Delta\mu_{H_2O}$, for which liquid water is in equilibrium with its vapour at $T = 298$ K. The variations of the two chemical potential were also recast into temperature scales at $p = 1$ atm and pressure scales at $T = 300$ K.

and Fe_3O_4 (Fig. 4) we identify five competing surfaces, corresponding to the clean $4f_2$ and 2b terminations, two hydroxilated 12k-O surfaces (the fully hydroxylated one, with four H atoms per surface unit cell (4H@12k-O), and the partially hydroxylated one, with three H atoms per surface unit cell (3H@12k-O)), and the hydroxilated $4f_2$ termination (OH+H@4f_2). In the limit of low water chemical potentials, *i.e., water poor* conditions, the clean 2b and $4f_2$ terminations are the preferred surfaces in the oxygen poor *versus* oxygen rich conditions (as discussed in the previous section and shown in Figs. 2 and 3). At higher values of the water chemical potential, there is an excess of hydrogen in the system, and the hydroxilated 4H@12k-O, 3H@12k-O and OH+H@4f_2 terminations become more stable. As depicted in Fig. 4, for a given value of the water chemical potential, going from oxygen rich conditions to oxygen poor conditions corresponds to a change in the stability domain between the *partially* hydroxylated 12k-O surface to the *fully* hydroxylated one.

By including a water reservoir in our investigation, we have shown that the fully or partially hydroxylated 12k-O terminations can display lower surface free energies than the *pristine* bulk terminations, thereby making them thermodynamically preferred under certain conditions. This analysis allows us to reinterpret the experimental characterization of the BHF platelets [7], for which a 12k/12k-O termination was identified in HAADF STEM images at Ba poor conditions. Notice, however, that because light elements like oxygen and hydrogen are not visible in HAADF STEM images, it is not possible to establish the degree of hydroxylation of the platelets nor to discern between the 12k and 12k-O terminations. Moreover, even if our results align well with the general trend observed in the BHF platelets, the correspondence between the *modelled* chemical conditions under which a BHF surface is the most stable and the *actual* environment of the platelets is more subtle. Our diagrams in Fig. 4 indeed sample a

8

wider range of chemical conditions with respect to the chemical environment of the platelets. For this reason, along the stability limit of iron oxides, we find five surfaces that are stable, compared to the single 12k (or 12k-O) proposed from HAADF STEM images at Ba poor conditions [7]. Note, however, that the pristine terminations (2b and $4f_2$) and the hydroxylated $4f_2$ termination are identified to be the most stable only when the water chemical potential is very low, corresponding to environments where only traces of water are present. Ruling out the *competing* surfaces, we can summarize that the hydroxylated 12k-O terminations are most likely present in Ba poor conditions, which is in line with experimental observations.

Additionally, we consider the annealing conditions of the platelets at 700°C, after which the 2b termination is *recovered*. By moving along the temperature scales in Fig. 4, we observe that at high temperatures the 2b termination is indeed the most stable in both surface diagrams. In particular, since the annealing of the platelets was performed in ambient air [7], we approximate these conditions by assuming an oxygen partial pressure of 0.2 atm and a partial pressure of water of 0.018 atm (corresponding to half the saturation water vapor pressure at standard conditions) at 1000 K. By using Eq. S3 in the Supplementary Material, the values of $\Delta\mu_O$ and $\Delta\mu_{H_2O}$ are −2.3 eV and −2.4 eV respectively. For these particular values of water and oxygen chemical potentials (not shown in Fig. 4) the 2b termination is truly the most stable.

In order to provide a better connection with experiments, which are typically performed in an aqueous solution, we employ the computational hydrogen electrode approach [15]. This approach relies on the fact that, by setting the reference potential to that of the standard hydrogen electrode (SHE), the cathode half-reaction,

$$\frac{1}{2}H_2 \rightarrow H^+ + e^-, \qquad (24)$$
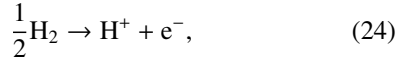
is in equilibrium when the pH of the electrolyte is equal to 0 and hydrogen gas is at standard conditions, *i.e.*, $T = 298$ K and $p = 1$ atm. At a pH different from zero, the free energy per H^+ cation is corrected by the concentration of cations, $\mu_{H^+} = kT \ln a_{H^+} = -kT \ln 10\text{pH}$. For an applied potential other than that of the SHE, the electrode bias contributes with $-eU_{SHE}$ to the reaction free energy. The chemical potential of hydrogen can then be written as [15],

$$\mu_H = \frac{1}{2}\mu_{H_2}^{gas} - kT\ln 10\text{pH} - eU_{SHE}, \qquad (25)$$

Where $\mu_{H_2}^{gas}$ is the chemical potential of molecular hydrogen at standard temperature-pressure conditions. Its value is approximated as the DFT total energy for an isolated H_2 molecule, corrected by the vibrational, rotational, and translational contributions to the free energy at standard conditions (see Section S1.2 in the Supplementary Material). The corresponding deviation of the hydrogen chemical potential, $\Delta\mu_H = \mu_H - \frac{1}{2}\mu_{H_2}^{gas}$, is then written in terms of the pH and the U_{SHE} potential,

$$\Delta\mu_H = -kT\ln 10\text{pH} - eU_{SHE}. \qquad (26)$$

The oxygen chemical potential can also be expressed as a function of the pH and the potential U_{SHE} by imposing Eq. 19. In this case, we fix the deviation of the water chemical potential to that of liquid water ($\mu_{H_2O}^{liquid}$), where we exploit the fact that liquid water is in equilibrium with its vapor phase at room temperature ($T =298$ K), with a vapor pressure of $p = 0.035$ atm,

$$\mu_{H_2O}^{liquid} = \mu_{H_2O}^{gas} + kT \ln \frac{p}{p_0}. \qquad (27)$$

The deviation of the oxygen chemical potential can then be written as,

$$\Delta\mu_O = \mu_{H_2O}^{liquid} - \mu_{H_2}^{gas} - \frac{1}{2}\mu_{O_2}^{gas} + 2kT \ln 10\text{pH} + 2eU_{SHE}. \qquad (28)$$

Given the new references for the water and oxygen chemical potentials (Eqs. 27, 28), we can compute the surface free energies in Eqs. 14, 15, 16 for a set of pH and U_{SHE} values. In Fig. 5, we show the most stable BHF surfaces as a function of the pH and the electrode potential, U_{SHE}. Along the barium oxide formation line, we identify two stability domains, corresponding to the pristine 2b termination and the hydroxilated 4H@12k-O surface. Similarly to the diagram in the $\Delta\mu_O - \Delta\mu_{H_2O}$ plane (Fig. 4), the hydroxilated surface is favored by the presence of hydrogen or at *acidic conditions* (low values of pH). In the case of the iron oxide stability lines, six different surfaces are identified as the most stable in the pH-U_{SHE} plane: the clean 2b and 12k-O surfaces and the hydroxylated OH+H@2b, 4H@12k-O, 3H@12k-O, and 2H@12k-O surfaces. Analogously to the plots in Fig. 4, the fully hydroxylated 12k-O surface is favored with respect to the partially hydroxylated one for higher values of the hydrogen chemical potential, *i.e.*, lower values of pH. In fact, notice that these diagrams correspond to the ones in the $\Delta\mu_O - \Delta\mu_{H_2O}$ plane for the constrained subspace indicated by the white dashed line in the plots in Fig. 4, representing the equilibrium between vapour and liquid water at standard conditions.

9

Along both formation lines, we do however sample a wider set of chemical conditions (or a larger set of $\Delta\mu_O$ values), within which, for example, the 12k-O termination becomes one of the preferred surfaces. By taking into consideration the evolution of hydrogen and oxygen (dashed lines in Fig. 5), we retrieve the formation limits of molecular oxygen and hydrogen.

The variation of the surface stability when the pH is tuned from basic to acidic conditions has been observed in the synthesis of the BHF platelets [7]. Indeed, the synthesis of these particles is performed in solution with NaOH, whereas washing the excess of barium in the sample is done with nitric acid.
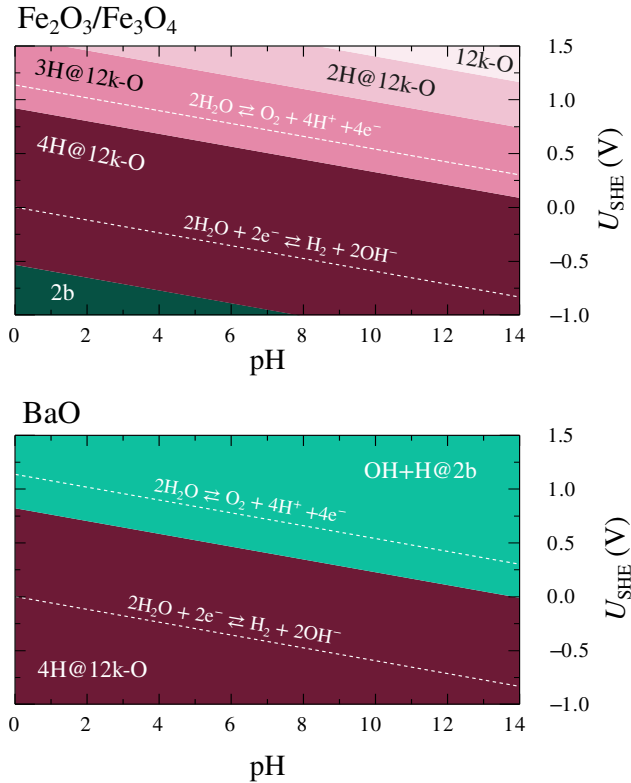
Figure 5: The 2b, 12k-O, OH+H@2b, 4H@12k-O, 3H@12k-O and 2H@12k-O terminations as the most stable BHF surfaces under specific pH and U_{SHE} conditions. On the upper panel, the iron chemical potential is constrained to the formation of iron oxides. On the lower panel, the surface free energies are estimated along the BaO stability line. The dashed lines represent the evolution of hydrogen and oxygen or the formation lines of molecular hydrogen and oxygen.

5. Conclusions

We performed an extensive investigation of the relative stability of BHF surfaces within the well-established *ab initio* thermodynamics framework under a wide range of chemical conditions. Given the five non-equivalent iron crystallographic sites, its non stoichiometric surfaces present a wide range of excess or deficit of barium, iron and oxygen and so, the respective surface free energies strongly depend on the chemical environment. More concretely, we consider all possible bulk terminations along the *c*-axis in contact with chemical reservoirs of iron and oxygen. We identified the 2b and the $4f_2$ terminations as the ones with the lowest surface free energies at Ba-rich *versus* Ba-poor conditions, respectively. In contact with an atmosphere containing water, three hydroxylated surfaces become the most stable at high values of the water chemical potential: the 4H@12k-O, the 3H@12k-O and the OH+H@2b. A final sampling of chemical conditions is performed by setting the reference of chemical potentials to the standard hydrogen electrode. This analysis reveals that going from a basic to an acidic environment the 4H@12k-O becomes more stable than OH+H@2b in Ba-rich conditions, whereas in Ba poor conditions the fully hydroxylated 4H@12k-O becomes preferred over 3H@12k-O.

Our model of BHF surfaces is in line with the surface variation observed in BHF platelets from HAADF STEM images [7]. After synthesis, at Ba-rich and basic conditions, a 2b termination is identified, whereas after washing the excess of Ba with nitridic acid, a 12k (12k-O) termination is proposed. From our *ab initio* calculations, we not only reproduce this trend, but we provide atomic scale detail of the surface morphology. In the case of Ba-poor and acidic conditions, our results strongly indicate that the 12k-O termination is preferred over the 12k termination. Moreover, we are in position to describe the level of hydroxylation of the clean terminations; the 12k-O surface is stabilized with three or four hydrogen atoms per surface unit cell. However, given that our *ab initio* thermodynamics framework is built in the high dimensional space of five chemical potentials, our results should not be interpreted for a specific set of chemical conditions, but they should read as general and grounded stability trends.

6. Acknowledgment

References

[1] R. C. Pullar, Hexagonal ferrites: A review of the synthesis, properties and applications of hexaferrite ceramics, Progress in Materials Science 57 (7) (2012) 1191–1334. doi:https://doi.org/10.1016/j.pmatsci.2012.04.001. URL https://www.sciencedirect.com/science/article/pii/S0079642512000369

[2] M. Koleva, P. Atanasov, R. Tomov, O. Vankov, C. Matin, C. Ristoscu, I. Mihailescu, D. Iorgov, S. Angelova, C. Ghelev, N. Mihailov, Pulsed laser deposition of barium hexaferrite (BaFe12O19) thin films, Appl. Surf. Sci. 154-155 (2000) 485–491. doi:10.1016/S0169-4332(99)00404-3.

[3] H. Xu, W. Zhang, B. Peng, W. Zhang, Properties of barium hexa-ferrite thin films dependent on sputtering pressure, Appl. Surf. Sci. 257 (7) (2011) 2689–2693. doi:10.1016/j.apsusc.2010.10.045.

[4] S. Meng, Z. Yue, X. Zhang, L. Li, Quasi-epitaxial barium hexaferrite thin films prepared by a topotactic reactive diffusion process, Appl. Surf. Sci. 290 (2014) 340–345. doi:10.1016/j.apsusc.2013.11.079.

[5] H.-B. Cho, M. Kanno, M. Lim, T. Nakayama, Y.-H. Choa, Design and synthesis of barium ferrite-based nanocomposite films with highly regulated 3-D structures, Appl. Surf. Sci. 555 (2021) 149515. doi:10.1016/j.apsusc.2021.149515.

[6] M. Drofenik, I. Ban, D. Makovec, A. Žnidaršič, Z. Jagličić, D. Hanžel, D. Lisjak, The hydrothermal synthesis of superparamagnetic barium hexaferrite particles, Mater. Chem. Phys. 127 (3) (2011) 415–419. doi:10.1016/j.matchemphys.2011.02.037.

[7] D. Makovec, B. Belec, T. Goršak, D. Lisjak, M. Komelj, G. Dražić, S. Gyergyek, Discrete evolution of the crystal structure during the growth of ba-hexaferrite nanoplatelets, Nanoscale 10 (2018) 14480–14491. doi:10.1039/C8NR03815E. URL http://dx.doi.org/10.1039/C8NR03815E

[8] A. Mertelj, D. Lisjak, M. Drofenik, M. Čopič, Ferromagnetism in suspensions of magnetic platelets in liquid crystal, Nature 504 (7479) (2013) 237–241. doi:10.1038/nature12863.

[9] G. Koplovitz, D. Primc, O. B. Dor, S. Yochelis, D. Rotem, D. Porath, Y. Paltiel, Magnetic Nanoplatelet-Based Spin Memory Device Operating at Ambient Temperatures, Adv. Mater. 29 (17) (2017) 1606748. doi:10.1002/adma.201606748.

[10] J. Hu, T. Gorsak, E. M. Rodríguez, D. Calle, T. Muñoz-Ortiz, D. Jaque, N. Fernández, L. Cussó, F. Rivero, R. A. Torres, J. G. Solé, A. Mertelj, D. Makovec, M. Desco, D. Lisjak, F. Alfonso, F. Sanz-Rodríguez, D. H. Ortgies, Magnetic Nanoplatelets for High Contrast Cardiovascular Imaging by Magnetically Modulated Optical Coherence Tomography, ChemPhotoChem 3 (7) (2019) 529–539. doi:10.1002/cptc.201900071.

[11] W. Wu, Q. He, C. Jiang, Magnetic Iron Oxide Nanoparticles: Synthesis and Surface Functionalization Strategies, Nanoscale Res. Lett. 3 (11) (2008) 397–415. doi:10.1007/s11671-008-9174-9.

[12] X. Tang, Y. Yang, Surface modification of M-Ba-ferrite powders by polyaniline: Towards improving microwave electromagnetic response, Appl. Surf. Sci. 255 (23) (2009) 9381–9385. doi:10.1016/j.apsusc.2009.07.040.

[13] D. Lisjak, S. Ovtar, J. Kovač, L. Gregoratti, B. Aleman, M. Amati, M. Fanetti, D. Makovec, A surface-chemistry study of barium ferrite nanoplates with DBSa-modified surfaces, Appl. Surf. Sci. 305 (2014) 366–374. doi:10.1016/j.apsusc.2014.03.092.

[14] K. Reuter, M. Scheffler, First-Principles Atomistic Thermodynamics for Oxidation Catalysis: Surface Phase Diagrams and Catalytically Interesting Regions, Phys. Rev. Lett. 90 (4) (2003) 046103. doi:10.1103/PhysRevLett.90.046103.

[15] J. K. Nørskov, J. Rossmeisl, A. Logadottir, L. Lindqvist, J. R. Kitchin, T. Bligaard, H. Jónsson, Origin of the overpotential for oxygen reduction at a fuel-cell cathode, The Journal of Physical Chemistry B 108 (46) (2004) 17886–17892. arXiv:https://doi.org/10.1021/jp047349j, doi:10.1021/jp047349j. URL https://doi.org/10.1021/jp047349j

[16] P. Giannozzi, S. Baroni, N. Bonini, M. Calandra, R. Car, C. Cavazzoni, D. Ceresoli, G. L. Chiarotti, M. Cococcioni, I. Dabo, A. Dal Corso, S. de Gironcoli, S. Fabris, G. Fratesi, R. Gebauer, U. Gerstmann, C. Gougoussis, A. Kokalj, M. Lazzeri, L. Martin-Samos, N. Marzari, F. Mauri, R. Mazzarello, S. Paolini, A. Pasquarello, L. Paulatto, C. Sbraccia, S. Scandolo, G. Sclauzero, A. P. Seitsonen, A. Smogunov, P. Umari, R. M. Wentzcovitch, QUANTUM ESPRESSO: a modular and open-source software project for quantum, J. Phys.: Condens. Matter 21 (39) (2009) 395502. doi:10.1088/0953-8984/21/39/395502.

[17] P. Giannozzi, O. Andreussi, T. Brumme, O. Bunau, M. B. Nardelli, M. Calandra, R. Car, C. Cavazzoni, D. Ceresoli, M. Cococcioni, N. Colonna, I. Carnimeo, A. Dal Corso, S. de Gironcoli, P. Delugas, R. A. DiStasio, A. Ferretti, A. Floris, G. Fratesi, G. Fugallo, R. Gebauer, U. Gerstmann, F. Giustino, T. Gorni, J. Jia, M. Kawamura, H.-Y. Ko, A. Kokalj, E. Küçükbenli, M. Lazzeri, M. Marsili, N. Marzari, F. Mauri, N. L. Nguyen, H.-V. Nguyen, A. Otero-de-la Roza, L. Paulatto, S. Poncé, D. Rocca, R. Sabatini, B. Santra, M. Schlipf, A. P. Seitsonen, A. Smogunov, I. Timrov, T. Thonhauser, P. Umari, N. Vast, X. Wu, S. Baroni, Advanced capabilities for materials modelling with Quantum ESPRESSO, J. Phys.: Condens. Matter 29 (46) (2017) 465901. doi:10.1088/1361-648X/aa8f79.

[18] J. P. Perdew, K. Burke, M. Ernzerhof, Generalized Gradient Approximation Made Simple, Phys. Rev. Lett. 77 (18) (1996) 3865–3868. doi:10.1103/PhysRevLett.77.3865.

[19] D. Vanderbilt, Soft self-consistent pseudopotentials in a generalized eigenvalue formalism, Phys. Rev. B 41 (11) (1990) 7892–7895(R). doi:10.1103/PhysRevB.41.7892.

[20] Pseudopotentials for Ba, Fe, O, H atoms were taken from the *Quantum Espresso PseudoPotential Download Page*: http://www.quantum-espresso.org/legacy_tables (files: Ba.pbe-spn-kjpaw_psl.1.0.0.UPF, Fe.pbe-nd-rrkjus.UPF, O.pbe-n-kjpaw_psl.1.0.0.UPF, H.pbe-rrkjus.UPF . (2023).

[21] H. J. Monkhorst, J. D. Pack, Special points for Brillouin-zone integrations, Phys. Rev. B 13 (12) (1976) 5188–5192. doi:10.1103/PhysRevB.13.5188.

[22] E. W. Gorter, Saturation magnetization of some ferrimagnetic oxides with hexagonal crystal structures, Proceedings of the IEE - Part B: Radio and Electronic Engineering 104 (5S) (1957) 255–260. doi:10.1049/pi-b-1.1957.0042.

[23] M. Cococcioni, S. de Gironcoli, Linear response approach to the calculation of the effective interaction parameters in the LDA+U

11

method, Phys. Rev. B 71 (3) (2005) 035105. `doi:10.1103/PhysRevB.71.035105`.

[24] I. Timrov, N. Marzari, M. Cococcioni, Hubbard parameters from density-functional perturbation theory, Phys. Rev. B 98 (8) (2018) 085127. `doi:10.1103/PhysRevB.98.085127`.

[25] C. M. Fang, F. Kools, R. Metselaar, G. de With, R. A. de Groot, Magnetic and electronic properties of strontium hexaferrite srfe12o19 from first-principles calculations, Journal of Physics: Condensed Matter 15 (36) (2003) 6229. `doi:10.1088/0953-8984/15/36/311`.
URL `https://dx.doi.org/10.1088/0953-8984/15/36/311`

[26] P. Novák, J. Rusz, Exchange interactions in barium hexaferrite, Phys. Rev. B 71 (2005) 184433. `doi:10.1103/PhysRevB.71.184433`.
URL `https://link.aps.org/doi/10.1103/PhysRevB.71.184433`

[27] C. Wu, Z. Yu, K. Sun, J. Nie, R. Guo, H. Liu, X. Jiang, Z. Lan, Calculation of exchange integrals and Curie temperature for La-substituted barium hexaferrites, Sci. Rep. 6 (36200) (2016) 1–8. `doi:10.1038/srep36200`.

[28] C. Tejera-Centeno, S. Gallego, J. I. Cerdá, An ab initio study of the magnetic properties of strontium hexaferrite, Sci. Rep. 11 (1964) (2021) 1–12. `doi:10.1038/s41598-021-81028-7`.

[29] C. Bhandari, M. E. Flatté, D. Paudyal, Enhanced magnetic anisotropy in lanthanum m-type hexaferrites by quantum-confined charge transfer, Phys. Rev. Materials 5 (2021) 094415. `doi:10.1103/PhysRevMaterials.5.094415`.
URL `https://link.aps.org/doi/10.1103/PhysRevMaterials.5.094415`

[30] A. Bañuelos-Frías, G. Martínez-Guajardo, L. Alvarado-Perea, L. Canizalez-Dávalos, F. Ruiz, C. Valero-Luna, Light absorption properties of mesoporous barium hexaferrite, BaFe12O19, Mater. Lett. 252 (2019) 239–243. `doi:10.1016/j.matlet.2019.05.137`.